Supplementary Information

Lenticular Hexagon-to-Hexagram Shape Transformation: Nano-Origami in Liquid Droplets

Catherine Quilliet,[1,*] Alexander V. Butenko,[2,3] and Eli Sloutskin[3,2,†]

[1] *CNRS/Université Grenoble-Alpes, LIPhy UMR 5588, Grenoble F-38401, France*

[2] *Bar-Ilan Institute of Nanotechnology & Advanced Materials, Bar-Ilan University, Ramat-Gan 5290002, Israel*

[3] *Physics Department, Bar-Ilan University, Ramat-Gan 5290002, Israel*

(Dated: December 8, 2025)

* Catherine.Quilliet@univ-grenoble-alpes.fr

† Eli.Sloutskin@biu.ac.il

I. EXPERIMENTAL HEXAGRAM OBSERVATIONS: OTHER MATERIALS

To test the generality of our observations, we performed additional measurements on three alkane–surfactant combinations beyond the hexadecane–trimethylammonium bromide system discussed in the main text. In all cases, lenticular hexagon droplets transformed into hexagrams upon reheating above T_{SE} (see Fig. S1). Although these systems do not exhaust the many alkane–surfactant combinations known to exhibit self-faceting[2, 3, 6-11, 15, 21-23, 26, 35], the results suggest that other self-faceting systems are likewise expected to show the hexagon-to-hexagram transition.

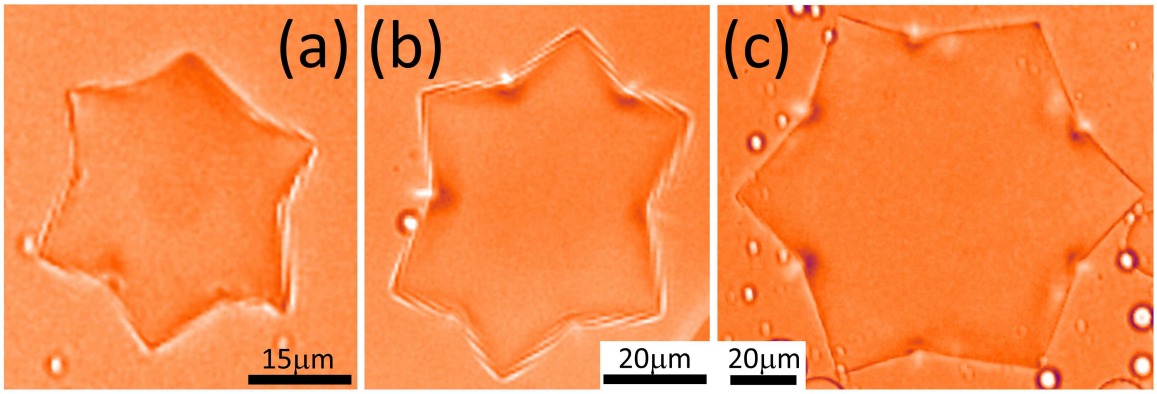

FIG. S1. Similar hexagram-shaped droplets are observed for (a) heptadecane [$H(CH_2)_{17}H$] alkane in a 1 mM octadecyltrimethylammonium bromide [$H(CH_2)_{18}(CH_3)_3NBr$] aqueous surfactant solution; (b) hexadecane [$H(CH_2)_{16}H$] in a 0.6 mM nonadecyltrimethylammonium bromide [$H(CH_2)_{19}(CH_3)_3NBr$] solution; and (c) hexadecane in a 10 mM Brij™-78 solution.

II. ORIGAMI MODEL GEOMETRY

To obtain the geometric relations presented in the main text, we first calculate the diameter D of our origami hexapita model (see Fig. 3(a)-(c) of the main text). For that, we note that the geodesic distances between points on the folded hexapita are the same as those measured on the initial hexagon, prior to folding. In particular, the side lengths a of the initial hexagon, the geodesic distance $\sqrt{3}R$ between the opposite permanent vertices, and

the geodesic distance $2R$ between the midpoints of two opposite sides remain unaffected by the folding. Thus:

$$D\left(R,\ell\right)=\sqrt{3}R\left[\ell^{\star}+\frac{2}{3}\sqrt{1-\frac{3}{4}\ell^{\star 2}}\right] \tag{1}$$

and the total volume of the inflated structure is:

$$V\left(R,\ell\right)=3\sqrt{3}R^{3}\times\ell^{\star}\left(1-\ell^{\star}\right)\left[\ell^{\star}+\frac{4}{9}\sqrt{1-\frac{3}{4}\ell^{\star 2}}\right]. \tag{2}$$

Here $\ell^{\star}=\ell/R$, with ℓ and R defined in Fig. 3 (main text). The folding corresponds to a decrease in $\ell^{\star}$ from 1 (flat pocket) to $\ell^{\star}=0$. This variation of $\ell^{\star}$ corresponds to an increase in volume from 0 to a maximum value V_{max}, followed by a decrease back to zero as $\ell^{\star}\to 0$ (Fig. S2), at which point the 6 pyramids degenerate into flattened vertical wings, and the central polygon collapses into a point (Fig. 3(g) of the main text).

For non-dimensionalization, we divide the volume of the hexapita (Eq. (2)) by $V_S=4R^3/\left(3^{1/4}\pi^{1/2}\right)$, which corresponds to the volume of a sphere having the same surface area as the initial undeformed hexapita. The resulting dimensionless volume is thus given by:

$$v\left(\ell^{\star}\right)=\frac{3^{7/4}\pi^{1/2}}{4}\ell^{\star}\left(1-\ell^{\star}\right)\left[\ell^{\star}+\frac{4}{9}\sqrt{1-\frac{3}{4}\ell^{\star 2}}\right]. \tag{3}$$

Notably, since the surface area of the origami hexapita is fixed, this dimensionless value simply equals to the compacity c introduced in the main text. By maximizing Eq. (3), we find the maximum dimensionless volume that can be contained in an inflatable hexagonal pocket, folded without stretch: $v_{max}=0.7126$, corresponding to $\ell^{\star}_{max}=0.5949$ (Fig. S2). Refining the origami model by allowing the facets to bend and stretch induces a dependence of the maximum volume on the pressure; nevertheless, it is possible to define a dimensionless filling volume to be compared with this v_{max} (see Section II.C below).

Among the different dimensionless features that can be measured in emulsion droplet movies, we choose the convexity angle α, defined in Fig. 3(b) of the main text, as it is non local, yet easily measured and almost unaffected by the focus of the imaging system. By simple geometry:

$$\alpha=\frac{2\pi}{3}-2\arctan\sqrt{\frac{4}{3\ell^{\star 2}}-1}, \tag{4}$$

demonstrating that α varies from $+\frac{\pi}{3}$ to $-\frac{\pi}{3}$ when $\ell^{\star}$ evolves from 1 to 0.

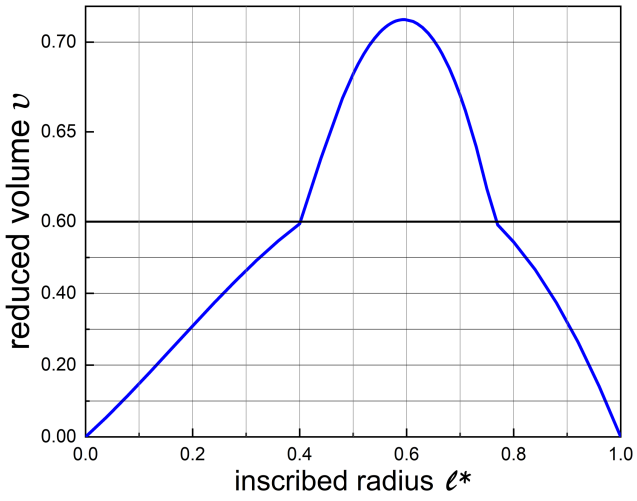

FIG. S2. The dimensionless volume of the origami hexapita model exhibits a peak $v_{max} = 0.7126$ for an optimal $\ell^\star = 0.5949$ value (Eq. (3)). Note the detailed y-scale for $v > 0.6$.

Since R is only directly measurable for a flat shape, $\ell^\star$ is not a convenient parameter to measure in experiments. Therefore, we use Eqs. (1) and (4) to obtain a direct relation between α and D/ℓ, which are readily measurable:

$$\frac{D}{2\ell} = \frac{\sqrt{3}}{2} + \sqrt{\frac{1}{3\ell^{\star 2}} - \frac{1}{4}} = \frac{\sqrt{3}}{2} + \frac{1}{2}\tan\left(\frac{\pi}{3} - \frac{\alpha}{2}\right). \tag{5}$$

Interestingly, when $\alpha = 0$, so that the horizontal projection of the inflated hexagon provides an exact 'Star of David' ('Magen David' and also the guild emblem of the brewers; Fig. 3(e) of the main text), $\ell = \frac{R}{\sqrt{3}}$, and the dimensionless volume is 0.7115, only a few ‰ smaller than the maximum volume.

Inverting Eq. (4), we obtain:

$$\ell^* = \frac{2}{\sqrt{3}}\cos\left(\frac{\pi}{3} - \frac{\alpha}{2}\right), \tag{6}$$

which allows the R value to be obtained directly from α and D:

$$R = \frac{D}{\ell^*\sqrt{3} + \sqrt{\frac{4}{3} - \ell^{*2}}}. \tag{7}$$

Note, that the surface area of a flat hexagonal pocket is given by $A = \left(\frac{6\sqrt{\pi}V}{v}\right)^{2/3}$, and in origami folding, A remains invariant. Therefore, for a given combination of D and α, this expression, together with Eqs. (2),(3), and (7), determines the value of A (i.e., the open symbols in Fig. 4(b) of the main text).

III. DROPLET SHAPE SIMULATIONS

A. Modeling the interfacial crystal as a thin elastic sheet

We complement the results of our origami calculations, using the softer (stretchable and bendable) model of the thin elastic interface, which is solved numerically [see main text, Fig. 2(c)-(d) and Fig. 4(a)]. For that purpose, the energy associated with tangential deformations of an isotropic 2D surface is characterized by a pair of 2D elastic parameters[51]: the 2D Young's modulus (Y) and the 2D Poisson's ratio (ν_{2D}). In addition, the bending modulus κ governs the out-of-plane deformations of this symmetric surface[42]. A thin sheet of "transversely isotropic" material[43], where the mechanical properties are locally invariant under rotations about the normal to the sheet, but may differ along the normal direction — such as in surfactant bilayers or monolayers — can similarly be modeled as a 2D isotropic elastic surface. However, in contrast to *fully-isotropic* thin sheets, the quantity $d = [12(1-\nu_{2D}^2)\kappa/Y]^{1/2}$ cannot be identified with the thickness of a *transversely isotropic* thin sheet[51]. Nevertheless, the corresponding dimensionless parameter, $d^\star \equiv d/R$, remains useful for our studies, as it characterizes the scale of the deformations[42]. Together, $d^\star$, ν_{2D}, and the dimensionless volume $v = 3^{1/4}\pi^{1/2}V/\left(4R^3\right)$, form a complete set of dimensionless control parameters that determine the energy landscape of our 2D surface.

B. Surface Evolver simulations: technical details

Our numerical simulations employ the Surface Evolver[40] finite element framework, using linear Hooke's law and assuming a linear elastic curvature response. Thus, the energy per unit surface area, minimized by Surface Evolver, is given by $e_{elast} = \frac{1}{2}\left(\kappa c^2 + \epsilon_{ij}K_{ijkl}\epsilon_{kl}\right)$, where ϵ_{ij} and K_{ijkl} are, respectively, the dimensionless surface Lagrangian finite strain tensor[52] (see details in Quilliet *et al.* [42] and the SI of Fierling *et al.* [41]) and the elasticity tensor[51]. Here, c is the mean curvature, whose integral over a sphere[53] is 16π.

To capture a broader range of deformations, the in-plane elasticity part $\frac{1}{2}\epsilon_{ij}K_{ijkl}\epsilon_{kl}$ was integrated on the undeformed surface, in a Lagrangian framework [40]. In our numerical calculations, the surface is discretized using a hexagonal mesh with 12288 facets. For each choice of internal volume, the bending and stretching of the surface were adjusted to minimize the energy. In some cases, the energy could be further reduced by additional inflation

followed by deflation, suggesting that this process helps the algorithm avoid local minima in the energy landscape. Due to the mesh resolution required for the modeling of thin hexapitas, the range of d^* could only be explored down to $d^* = 0.005$. Note that even more complex shapes may emerge at lower d^* values, although significantly greater computational power would be required to carry out simulations in this regime.

C. Pressure simulations and filling volume

In our Surface Evolver simulations, the volume enclosed by the 2D surface is an externally controlled parameter, so the simulations yield the difference between internal and external pressure: $P = \frac{\partial E_{elast}}{\partial V} = \frac{\partial}{\partial V}\left(\iint e_{elast}\right)$, obtained as the Lagrange multiplier. The corresponding dimensionless quantity, $P_{\text{adim}} = \frac{P}{d^* Y_{3D}} = \frac{RP}{Y}$, where Y_{3D} is the 3D Young's modulus, increases non-linearly as a function of v (see Fig. S3).

The dimensionless parameters P_{adim} and v enable comparison of pressure curves across high ($d^\star \geq 0.03$) and low ($d^\star \leq 0.02$) ranges of $d^\star$ values. As mentioned in the main text, the hexagon-to-hexagram transition occurs at low $d^\star$, while the high-$d^\star$ hexagons expand continuously, without any shape transitions (Fig. S4(a)-(b)). The low-v range of the $P_{\text{adim}}(v)$ curve is dominated by the bending energy, so that the pressure hardly varies. Buckling corresponds to a jump in pressure which happens only for the low-$d^\star$ hexapita (Fig. S3, inset). In the high-v range of the curve, pressure significantly increases. In this regime, dominated by the stretching energy, the curves obtained for both $d^\star = 0.01$ and $d^\star = 0.03$ almost perfectly overlap. Furthermore, a quasi-linear evolution takes place in this v-range, with a slope of order 1 obtained at high v, where the shape is near-spherical. This linear part defines the 'filling volume' $v_{\texttt{fill}}$ as the intersection of the linear fit to $P_{\text{adim}}(v)$ and the $P = 0$ axis. The same value of $v_{\texttt{fill}}$ is obtained for both the low- and the high- $d^\star$ ranges, indicating that the noticeable 3D shape difference between these two situations has only a negligible influence on the energies at stake. As expected, the filling volume $v_{\texttt{fill}} = 0.84$ is comparable to, and slightly exceeds, the maximum reduced volume $v_{max} = 0.7126$ of the origami model.

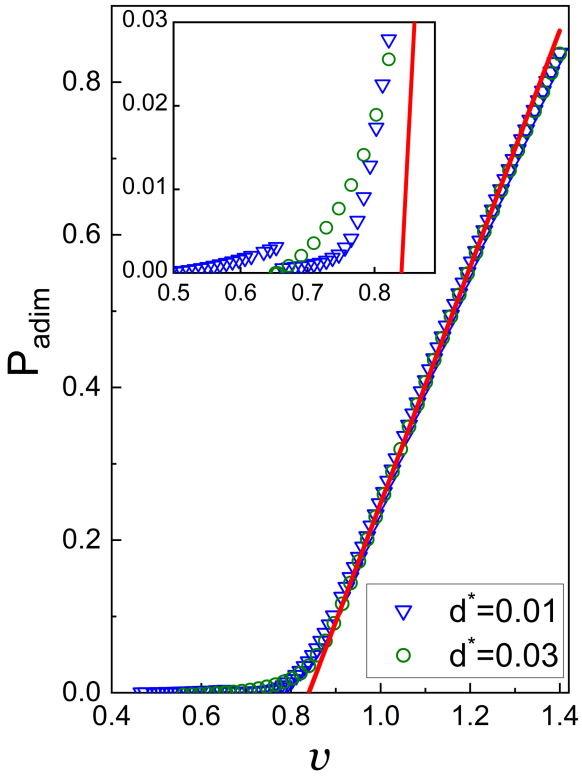

FIG. S3. Dimensionless pressure $P_{\text{adim}} = PR/Y$ as a function of the dimensionless volume v of an inflated elastic hexapita, as obtained from numerical Surface Evolver simulations. A continuous increase is observed for $d^* = 0.03$ (green circles), where no abrupt shape transitions occur. The abrupt pressure decrease at $v \approx 0.66$, observed for $d^* = 0.01$ (blue triangles) corresponds to the hexagon-to-hexagram buckling transition (see the inset for a magnified plot in the near-transition region). A linear fit to the $P_{\text{adim}}(v)$ dependence at high v extrapolates to $P = 0$ at $v = 0.840$, defined as the filling volume $v_{\texttt{fill}}$. $\nu_{2D} = 0.5$ is adopted in these calculations.

D. Fold size in simulated and experimental hexagrams

Upon transitioning to a lenticular hexagram shape, the numerically simulated surfaces develop folds midway between the vertices, closely resembling those observed in macroscopic experiments and emulsion droplets (Fig. 1 and 2 of the main text), in support of our proposed self-folding mechanism. Moreover, both simulations and macroscopic experiments allow precise quantification of fold size, as shown in Fig. S5(a), where a magnified view of the fold region is provided. Remarkably, the dimensionless parameter describing the fold size, $x^\star = x/R$, increases linearly with $d^\star$, in both numerical simulations and experiments (cf.

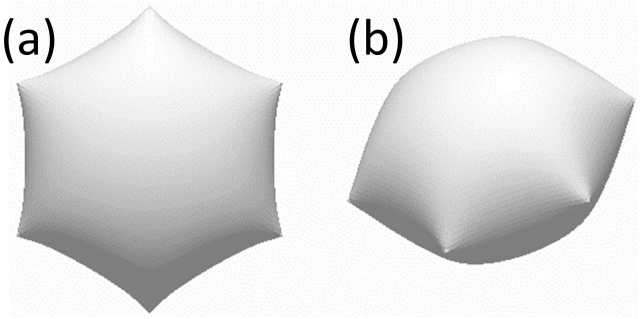

FIG. S4. (a) Top and (b) perspective views of a simulated droplet with $d^\star = 0.03$, $\nu_{2D} = 0.5$, and $v = 1.381$. At this high $d^\star$, no shape transformation occurs. At this high $d^\star$, the conformation for weak inflation is very similar to that of low-$d^\star$ objects, such as in Fig. 2(c) of the main text, but no shape transformation into a hexagram occurs upon further inflation.

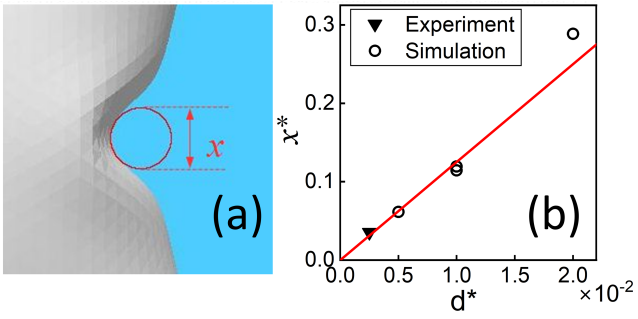

FIG. S5. (a) The size of the fold, which forms midway between the vertices in both simulations and experiments, is quantified by fitting a tangent circle of diameter x to its inner part. (b) The dimensionless parameter $x^\star \equiv x/R$ increases linearly with $d^\star$.

circles and triangles in Fig. S5(b)). The corresponding linear fit gives: $x^* \cong 0.68\, d^*$. The observed agreement between experiments and simulations strongly supports the validity of our 2D elastic model.

IV. MEASUREMENT OF HEXAGRAM SHAPE DESCRIPTORS (α AND D)

A. Experimental microscopy images

To measure D from a microscopy image of an emulsion droplet, we fit a nearly circular circumscribed ellipse to the vertices of the droplet. The area of this ellipse, A_{EL}, is measured, yielding $D = (4\pi A_{\text{EL}})^{1/2}$. The same procedure, with an inscribed ellipse rather than

a circumscribed one, is used to determined the value of 2ℓ. The value of α is obtained by measuring the angle between lines manually fitted to two edges (as shown in Fig. 1(c) of the main text). For each hexagram, we repeat this measurement for all six possible choices of α, taking the average value and the standard error of the mean.

B. Simulated droplets

The same procedure is applied to measure D and 2ℓ of the simulated droplets. The edges of the simulated droplets are somewhat less linear, than the experimental ones. Therefore, we performed precise edge detection using ChatGPT AI, verifying the accuracy of the edge detection by overlaying the detected edges onto the image of the simulated droplet. We then used automatic linear fits (in OriginLab™ software) to each of the 12 detected edges, allowing the α angles to be determined. As with the experimental data, we calculate the average of the six α values for each simulated droplet. However, the standard error of the mean is totally negligible here due to the near-perfect symmetry of the simulated shapes.

SUPPLEMENTARY VIDEO CAPTIONS

Video S1. A temperature scan of oil-in-water emulsion droplets, imaged via bright-field microscopy, shows a large droplet undergoing a sequence of shape transformations. Upon cooling, the droplet transitions from a sphere to an icosahedron, which then flattens into a lenticular hexagonal shape. On heating, the lenticular hexagon transforms into a hexagram before returning to a sphere. Black arrows indicate folds that emerge midway between the hexagram's vertices. These folds resemble those observed in the macroscopic model and simulation (Fig. 2(b) and 2(d) of the main text). Since smaller droplets have a higher transition temperature, a text label appears when the central droplet crosses T_{SE} during both cooling and heating. A pause symbol is displayed at the bottom during pauses, and the 'glow' LUT is applied throughout for enhanced visualization. The small shift between the observed sphere-to-icosahedron and hexagram-to-sphere transition temperatures is mainly–if not entirely–caused by thermal lag; extrapolation to zero scan rate reduces the difference to 0.14 ± 0.06°C. Importantly, both transitions occur several degrees below the interfacial freezing temperature T_s [2,19] (see main text).